Measurement of the thermal accommodation coefficient of helium on a crystalline silicon surface at low-temperatures

OPEN ACCESS
IOP Publishing
Classical and Quantum Gravity
Class. Quantum Grav. **41** (2024) 195013 (11pp) https://doi.org/10.1088/1361-6382/ad7184

Measurement of the thermal accommodation coefficient of helium on a crystalline silicon surface at low-temperatures

Alexander Franke[1,*], Nils Sültmann[1], Christoph Reinhardt[2], Sandy Croatto[2], Jörn Schaffran[2], Hossein Masalehdan[1], Axel Lindner[2] and Roman Schnabel[1]

[1] Institut für Quantenphysik und Zentrum für Optische Quantentechnologien, Universität Hamburg, 22761 Hamburg, Germany
[2] Deutsches Elektronen-Synchrotron DESY, Notkestr. 85, 22607 Hamburg, Germany

E-mail: afranke@physnet.uni-hamburg.de

Received 4 March 2024; revised 17 June 2024
Accepted for publication 20 August 2024
Published 3 September 2024

Abstract

Proposals for next-generation gravitational wave observatories include cryogenically cooled 200 kg test mass mirrors suspended from pendulums and made of a crystalline material such as crystalline silicon. During operation of the observatories, these mirrors undergo heating due to the absorption of laser radiation of up to a watt. Low noise cooling techniques need to be developed. Low-pressure helium exchange gas at 5 K might contribute to the challenging task. Here, we report the measurement of the helium accommodation coefficient $\alpha(11\,\mathrm{K} < T < 30\,\mathrm{K})$, which is the probability that a helium atom thermalises with a surface at a given temperature when reflected from it. We find $\alpha(T) > 0.7$ for temperatures $<20\,\mathrm{K}$, which increases the cooling power compared to recently used assumptions. The idea of free molecular flow helium

* Author to whom any correspondence should be addressed.

gas cooling is thus supported and might find application in some observatory concepts.

Keywords: experimental gravitation, cryogenics, gas cooling, gravitational wave detection, accommodation coefficient

1. Introduction

The first observation of gravitational waves (GW) [1] marked the beginning of a new chapter in astronomy and cosmology, as GW detection offers a new way to study the Universe alongside traditional telescope observations. Fast-forward to today, several improvements to the detectors [2–4] have been implemented. These sensitivity improvements contributed to many more event detections, thereby providing valuable information about the number density of black holes [5], the GW background [6], and an independently derived value of the rate at which the Universe is expanding (Hubble constant H_0) [7].

With next-generation interferometers [8–14], further improvements in the sensitivity are targeted. With the detection of weaker signals, we can potentially gain knowledge about gravity, the structure of spacetime, supernovae, compact binary systems long before they merge, and cosmic inflation. To this end, the design plans consider cooling the laser mirrors and test masses of space-time (TMs), which are of the order of 100 kg and suspended as pendulums, to cryogenic temperatures. On the one hand, this is aimed at suppressing thermal noise, which is currently limiting in the range from 40 Hz to 100 Hz [15, 16]. On the other hand, this might enable higher light powers [11] thereby reducing shot noise, which is limiting above 100 Hz.

Today the Japanese KAGRA observatory [4, 17], which began initial observations in Feb 2020 [18], will finally exploit mirrors cooled to about 20 K. The designs of the European Einstein Telescope and LIGO Voyager incorporate cryo-cooling as well. The ET pathfinder project is currently evaluating different cryogenic configurations for the Einstein Telescope [19, 20] aiming at either 123 K or 18 K.

The mirrors in the arm cavities are suspended on meter-scale, thin wires, behaving like the well-understood *harmonic oscillator*: disturbances above the resonance frequency are significantly reduced in amplitude. However, this excellent mechanical isolation comes with the drawback of substantial thermal isolation, as thin wires only conduct a very limited amount of heat. To reduce quantum shot noise, interferometric detectors need to use high-power lasers, which heat up mirror coatings and substrates. This thermal noise partially limits future observatories.

In a previous article [21], we proposed cooling the mirrors of a GW detector with a 5 K-helium gas at low pressure in the molecular flow regime. We showed that the momentum transfer results in an additional mirror displacement noise that is proportional to f^{-2}, where f is the GW frequency. We concluded that gas cooling is particularly suitable for observatories aiming to detect events in the kilohertz range, such as the Neutron Star Extreme Matter Observatory (NEMO) [11].

The effectiveness of gas cooling depends on the thermal accommodation coefficient α, which represents the fraction of the incident gas particles that thermalise with the TM. Its value depends on the type of gas, surface material, and temperature. For helium, $\alpha = 0.43$ has been measured at room temperature [22]. At 20 K, $\alpha = 0.6$ has been estimated, based on measurements with glass, platinum, and nickel surfaces [23]. Here, we measure the thermal accommodation coefficient of helium on crystalline silicon between 11 K and 30 K.

2. Heat transfer in gases

The heat transfer of gases confined in a volume is dependent on the mean free path λ compared to the wall-to-wall distance d. The Knudsen number $K_n = \lambda d^{-1}$ defines three regimes: viscous flow ($K_n \ll 1$), free molecular ($K_n \gg 1$), and transitional flow in between.

2.1. Gas cooling in the viscous flow regime

At ambient pressures, the presence of molecular collisions and momentum transfer between gas molecules almost always dominate the behavior of gases. This regime of gas dynamics is called *viscous flow* or continuous flow. Here, the heat transfer of gas between two identical, parallel plates of area A, separated by distance d is given by

$$P_{\mathrm{VF}} = \frac{\kappa(T) A \Delta T}{d} \qquad \text{if } \lambda \ll d, \tag{1}$$

with the temperature-dependent thermal conductivity of the gas κ, and temperature difference of the plates ΔT.

For $\lambda \approx d$, wall-molecule-interactions start to influence heat transfer. For $\lambda \gg d$, gas molecules rarely collide with each other, leading to more frequent thermal energy transfers with the walls.

2.2. Gas cooling in the free molecular flow regime

The heat transfer in the free molecular flow is additionally influenced by the surface material. The energy accommodation coefficient $\alpha \in [0, 1]$ accumulates these properties in a probability: Complete thermal equilibration at every molecule-surface interaction translates to $\alpha = 1$, no thermal exchange at any interaction translates to $\alpha = 0$ [23]. This coefficient is dependent on the gas type and surface material, and varies with temperature.

With the assumption of the colder plate satisfying $\alpha = 1$, the gas cooling power in the free molecular flow regime is given by [24]:

$$P_{\mathrm{fMF}} = \alpha(T) \sqrt{\frac{8 k_{\mathrm{B}}}{\pi m_{\mathrm{Gas}} T_{\mathrm{cold}}}} p A \Delta T \tag{2}$$

with energy accommodation coefficient of the hot surface α, mass of a gas molecule m_{Gas}, gas pressure at the colder surface p, and area of a single plate A. For copper surfaces and temperatures significantly below 10 K, the accommodation coefficient is close to unity [23].

3. Setup for measuring $\alpha_{\mathrm{He,cSi}}(11\,\mathrm{K} < T < 30\,\mathrm{K})$

A cylindrical, crystalline silicon test mass was placed inside an indium-sealed, vacuum chamber with a wall temperature of 10 K or less and adjustable helium pressure. A laser enabled us to deposit a known, tunable amount of heat energy in the test mass. To reach cryogenic temperatures, the aforementioned *inner chamber* is mounted to a cold plate inside a bigger *outer chamber*, which could be pumped to pressures below 10^{-8} mbar. A thermal shield surrounded the inner chamber to reduce radiative heating. This setup (shown in more detail in figure 1) enabled us to reach silicon surface temperatures of 11–30 K, which covers most of the suggested cryogenic detector designs mentioned in the introduction.

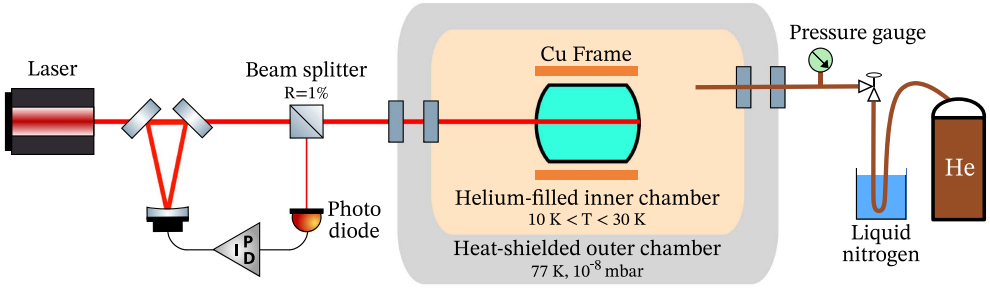

Figure 1. Simplified experimental setup. In order to measure $\alpha_{\mathrm{He,cSi}}(11\,\mathrm{K} < T < 30\,\mathrm{K})$, we place a cylindrical Si crystal (cyan) inside a helium-tight chamber (light orange), which is thermally connected to a cryogenically cooled plate. A power-adjustable laser (red) is guided through a pre-mode cleaner and a fiber for controlled heating of the test mass. We stabilize the light power, by splitting off 1% of power and directing it onto a photodiode. The output signal from the photodiode is used to control the light power allowed to pass the pre-mode-cleaner, which achieves reasonable power stability by using a variable offset DC-Lock. Optical power seen by the silicon TM fluctuates $<0.6\%$ during measurements. See section 4.3 for a description of the calibration of the absorbed power inside the test mass. Helium from a pressurized gas bottle (brown) with purity of 99.999% is guided through liquid nitrogen to remove contaminations. A variable leak rate valve controls the gas pressure measured by the gauge (green). A capillary connects inner chamber and pressure gauge.

We used a crystalline silicon cylinder made with the Czochralski technique [25] that was cut to have a diameter of (2.4863 ± 0.0024) cm and a length of (9.972 ± 0.004) cm. The test mass was held inside a polished copper frame almost fully enclosing it. The frame was fabricated to be equidistant to all silicone surfaces. This controlled distance of 2 mm is necessary to ensure compatibility with the free molecular flow regime requirement. Differences in thermal expansion of copper and silicon are insignificant [26, 27]. Six polytetrafluoroethylene (PTFE) screws with pointy tips held the test mass in the center of the frame. PTFE is known for its low thermal conductivity [28]. Thermal sensors were mounted to the test mass and the frame to measure their respective temperatures. Without any additional heat load, the test mass could be cooled to 7 K with similar frame temperatures.

Both chambers had optical ports. These allowed pointing a laser beam at wavelength 1064 nm onto the test mass. A capillary thermally anchored over a length of around 80 cm to the heat shield connects the inner chamber to the gas handling at room temperature. The ingoing laser power was held stable by a control loop with long-term stability. Additionally, this control loop allowed us to automatically heat the test mass to a desired temperature. Once the system reached equilibrium, data was collected for up to 30 min, where the following equation connects optical heating power P_{optH} and gas cooling power P_{gasC}:

$$P_{\mathrm{optH}} = P_{\mathrm{gasC}} + \Delta P_{\mathrm{res}} \tag{3}$$

where ΔP_{res} contains any remaining heat flow channels. P_{optH} is proportional to the input laser power. The light-power calibration is described in section 4.3. The value of P_{gasC} is dependent on the gas pressure, and in the case of molecular flow: the accommodation coefficient. ΔP_{res} is discussed in section 4.4. A front view of the system in the inner chamber is shown in figure 2.

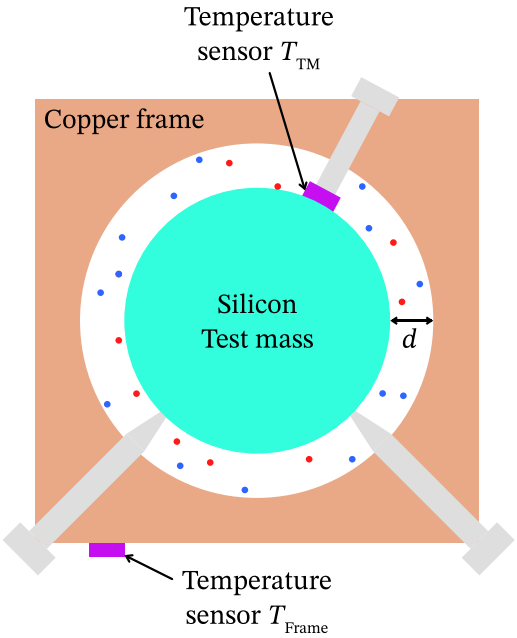

Figure 2. Cross section of the silicon cylinder (cyan) and its surrounding copper frame (orange). The silicon cylinder is held in place by six PTFE screws (light gray) with a distance to the frame of $d = 2$ mm. PTFE was chosen for its low thermal conductivity. For a similar reason, the tips are pointy. Thin film resistance sensors (purple) allow precise temperature readout. A seventh screw pushes one of the sensors onto the test mass. Alongside thermal grease, this allows for great thermal contact to ensure the sensor shows the test mass temperature as precisely as possible. Helium atoms (small red and blue dots) with different temperatures (T_{TM} and T_{frame}) at a pressure p_c exchange heat between frame and test mass.

4. Measurement of the thermal accommodation coefficient

4.1. Pressure measurement

The experiment operated in three gas pressure regimes: no-gas ($K_n \gg 10$), gas in molecular flow ($8 < K_n < 12$) and gas in viscous flow ($K_n < 0.01$). During individual measurements, helium inlet valve was closed; hence the pressure was static. The first and last regimes are needed for calibration: Measurement without gas allows for the determination of any unwanted heat flux (see section 4.4). Gas-cooling power in viscous flow is known (see equation (1)) and enables a precise calibration of the applied heating power (see section 4.3). With that, cooling power in molecular flow is proportional to one last unknown: the accommodation coefficient.

At the state of planning, no commercial pressure sensor for cryogenic temperatures was available to us. As a workaround, we connected the inner chamber via a capillary to a gas-type independent pressure gauge outside the cryostat. This capillary introduced a small heat bridge and therefore limited the minimum achievable temperature. Due to the *thermomolecular pressure difference effect*, a correction to the pressure readout needed to be applied. Given that the gas in the capillary was in molecular flow, the pressure readout in the warm region p_{w}

at temperature T_w could be measured and translated to the pressure inside the cryostat p_c at temperature T_c with:

$$\frac{p_\mathrm{c}}{p_\mathrm{w}} = \sqrt{\frac{T_\mathrm{c}}{T_\mathrm{w}}}. \tag{4}$$

At temperatures of 8 K, the pressure inside the inner chamber was approximately six times lower than at the pressure gauge. The required room temperature measurements added another small uncertainty of 3%–4% to the determined accommodation coefficients.

For a gas-type independent readout, we used a commercially available capacitive pressure transmitter. By design, these pressure gauges have the smallest uncertainty at the upper end of their sensitivity range. Consequently, we operated the experiment between $K_n = 8$ and $K_n = 12$ during molecular flow measurements. In testing, we found that zeroing of the sensor every 48 hours is necessary as the readout value drifted. Zeroing had to be executed at low pressures, in our case at $p < 10^{-6}$ mbar. Hence, the gas filled part of the experiment outside the cryostat gets pumped and flushed with fresh helium every two days. This had the added benefit that we ensured high-level purity of helium at all times.

4.2. Temperature measurement

Temperatures of the test mass (T_TM) and surrounding frame (T_frame) were read out with *negative temperature coefficient (NTC) resistor sensors*. A sensor (model Cernox 1070 HT sensor in CU package) was attached to the copper frame. Thermal grease and a hand-tight brass screw ensured good thermal contact. The cylindrical test mass was thermally well insulated from the cold copper. Its sensor (model Cernox 1070 HT sensor in SD package) may not be fixed to a flat surface, as laser light would heat it up if placed on one end of the cylinder. We chose a sensor assembled in a 3 mm × 2 mm rectangular package with about 1 mm height. A PTFE screw with bad thermal conductance pressed the flat surface of the sensor onto the curved test mass (see figure 2).

The temperature sensor controller unit applied temperature-dependent excitation current to each sensor to read out their electrical resistance. The readout showed only the voltage drop over the sensor, as we used a four-wire scheme making wire resistance irrelevant. Lake shore Cryotronics calibrated each the temperature against the International Temperature Scale of 1990 (ITS-90). They used platinum, rhodium–iron, and germanium resistance thermometers as reference and provided Chebychev polynomials for each sensor individually. For all sensors, the given deviations of less than 8 mK between 10 K–30 K to the reference thermometers were almost negligible for our evaluation (see figure 5).

A small electrical self-heating at each sensor was technically unavoidable. This heating was notable at the test mass sensor, as it was highly insulated from the cold plate of the cryostat. The electrical self-heating power was temperature-dependent, as with changing sensor resistance, the electrical current is also changing.

In the no-gas (molecular flow) [viscous flow] regime, we observed stable temperature readout differences between test mass and frame sensor of 757 mK (36 mK) [31 mK]. These differences were measured when all optical accesses to the test mass were blocked and no heat load other than sensor heating was present at the test mass. This showed a strong dependence of the temperature differences on gas pressure. Gas was exchanging heat between the test mass sensor and both the frame and test mass. Several numerical and experimental tests after the

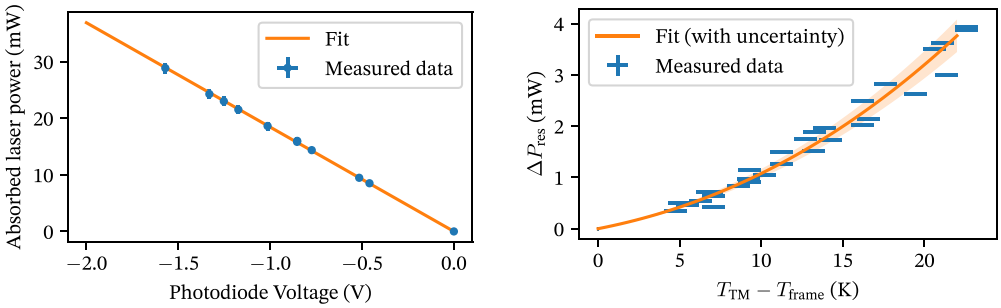

Figure 3. Left: a small, fixed portion of the laser light heating the test mass, is directed on a photodiode. The linear correlation between the voltage readout of this diode and absorbed laser power in the test mass is shown here. Data taken with gas in the viscous flow regime, where gas cooling is dominating and known (equation (1)). Right: residual cooling power of every heat flux channel apart from gas cooling ΔP_{res}. This is dominated by the heat conduction through the screws holding the test mass in place. Measured at pressures well below 10^{-6} mbar, where no cooling by gas contributes significantly to the heat flux of the test mass. The high temperature uncertainty is explained in section 4.2.

experiment run revealed that the readout of the test mass sensor has a high dependence on the specific mounting procedure and gas pressure. We suspect a heat accumulation inside the sensor, which was most notable in the no gas configuration, as the helium greatly increases the thermal contact between resistor and test mass surface. To compensate, we subtracted test mass temperature readings by above-mentioned values in dependence of the gas regime. At the same time, we continued with a systematic uncertainty equally to the subtracted amount. This fact had an influence on our no-gas calibration measurements determining ΔP_{res}, and the large uncertainty on temperature measurements during the calibration can be seen figure 3 right. Error propagation dictated higher uncertainties in the accommodation coefficient for experiment configurations at temperatures below 14 K.

4.3. Calibration of the absorbed optical power

A laser of wavelength 1064 nm deposited an adjustable and stable amount of thermal energy inside the test mass.

The end surfaces of the cylinder were polished and coated. For this experiment, it is irrelevant if the light is absorbed in the coatings or the bulk. COMSOL Multiphysics simulations have shown that the temperature inside the test mass is always nearly uniform, due to the high thermal conduction of silicon.

A beam splitter split off 1% of laser light just before the vacuum chamber which we guided onto a photodiode. The photovoltage provided feedback to a pre-mode-cleaner to compensate for thermal drifts in the laser system and therefore to ensure a stable heating power.

We determined the exact amount of optical heating applied to the test mass P_{optH}. Measuring incoming, reflected, and transmitted optical power proved to be nearly impossible, especially as the test mass does not form a cavity and optical scattering far off the laser axis occurred. The test mass position could not be adjusted in its position or angle once the vacuum chamber was closed (see figure 1). However, we correlated the photovoltage (used to stabilize laser power) to the actual light power absorbed in the test mass. The cooling performance of helium is well

known in the regime of viscous flow (see equation (1)). If we assume viscous cooling P_{VF} dominates and the test mass temperature is constant, we can directly calibrate photovoltage with $P_{\mathrm{gasC}} = P_{\mathrm{VF}} = P_{\mathrm{optH}}$. The results of this calibration are shown in figure 3(left).

4.4. Unwanted heat flux

We could not mount our test mass in such a way, that it was thermally fully decoupled from its environment, and cooling channels apart from gas-cooling remained. Our test mass was held in place by screws with low thermal conductivity, but nevertheless, some Milliwatts were cooled by conduction through these. An upper limit for heating power by thermal conduction through N_{s} screws of diameter d_{s}, temperature dependent thermal conductivity of teflon $\kappa_{\mathrm{s}}(T)$ [28], and length l is given by [29]:

$$P_{\mathrm{cond}}^{\mathrm{screws}} = \frac{N_{\mathrm{s}}\kappa_{\mathrm{s}}(T)}{l}\frac{\pi d_{\mathrm{s}}^2}{4}\Delta T. \tag{5}$$

Contact resistance and pointy tips reduced the actual conductivity.

Other thermal channels included radiation cooling to the copper frame, sensor self-heating, and radiation heating from the cryostat's heat shield (77 K). For our measurements with helium in the free molecular flow regime, the sum of all discommoding heat flux channels ΔP_{res} needed to be determined, to not miscalculate gas-cooling efficiency and hence the accommodation coefficient.

With precise knowledge of the absorbed laser power P_{optH} (see section 4.3) we determined any discommoding cooling with the helium chamber at pressure of way below 10^{-6} mbar. In this pressure regime, $P_{\mathrm{gasC}} = 0$ held true, and at constant test mass temperature, we had $\Delta P_{\mathrm{res}} = P_{\mathrm{optH}}$. The results are shown in figure 3(right).

4.5. Extracting the accommodation coefficient

Accommodation coefficients were measured with gas pressures in the molecular flow regime. From equation (3) we have

$$P_{\mathrm{optH}} = P_{\mathrm{fMF}} + \Delta P_{\mathrm{res}}. \tag{6}$$

with the free molecular flow cooling power P_{fMF}. Rearranging equation (2) yields

$$\alpha_{\mathrm{Si}} = \frac{P_{\mathrm{optH}} - \Delta P_{\mathrm{res}}}{p_{\mathrm{c}} A \Delta T} \cdot \sqrt{\frac{\pi m_{\mathrm{helium}} T_{\mathrm{frame}}}{8 k_{\mathrm{B}}}} \tag{7}$$

with $\Delta T = T_{\mathrm{TM}} - T_{\mathrm{frame}}$, the gas pressure around the test mass p_{c}, surface area of the test mass A, molar mass of Helium m_{helium}, and Boltzmann constant k_{B}.

Evaluating the above equation for different laser input powers yields the accommodation for different silicon temperatures. Measured data points alongside a fit are shown in figure 4.

Uncertainties in our measurements of the accommodation coefficient are dominated by a systematic error in the pressure readout, which is given by the technical limitations of the gauge. A detailed breakdown of all uncertainties is shown in figure 5.

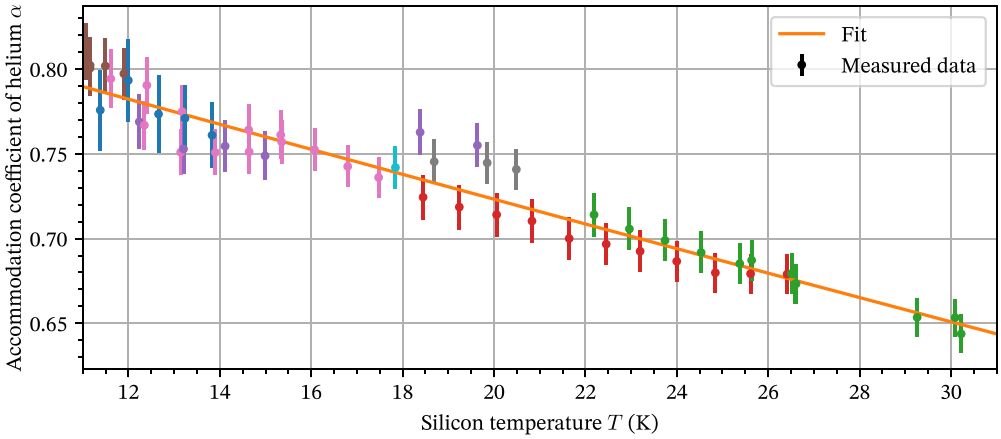

Figure 4. Measured accommodation coefficients of helium on a silicon surface at temperature T. Result of orthogonal distance regression in orange with $\alpha(T) = a + e^{b(T+c)}/(1+e^{b(T+c)})$. $a = -1.46 \cdot 10^{-1}, b = -1.47 \cdot 10^{-2}, c = -4.71 \cdot 10^{-4}$K. The color coding of the measured data points represents consecutive measurement runs only changing test mass temperature by adjusting laser power. In between runs, the pressure gauge was zeroed, and all gas in the room temperature division of the experiment was exchanged with fresh helium to ensure that no air contamination was manipulating the pressure readout. Additionally, we adjusted helium pressure to be compatible with the free molecular flow (Knudsen number >8) but as high as possible to reduce readout uncertainty.

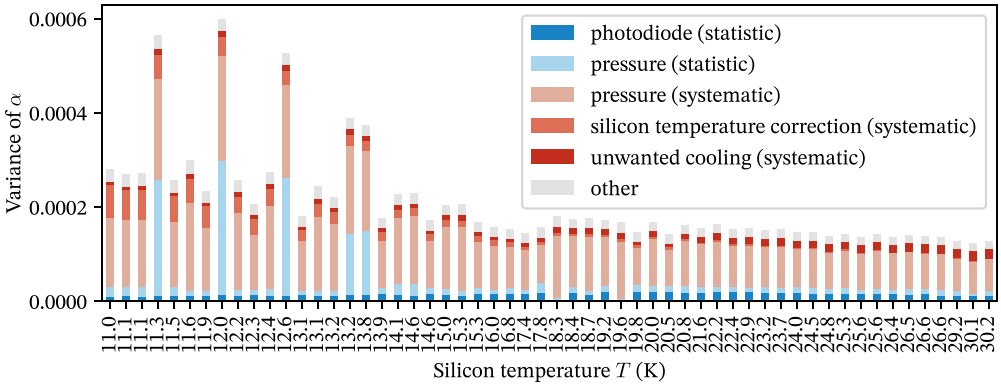

Figure 5. Uncertainites corresponding to data in figure 4. Plotted is the squared standard deviation. 'Other' is the sum of variances from the following sources: test mass temperature sensor (statistic and systematic), frame temperature sensor (statistic and systematic), laboratory temperature, test mass diameter and thickness, and photodiode calibration (see section 4.3).

5. Conclusion

We have designed and executed an experiment for determination of the helium accommodation coefficient at cryogenic temperatures. We covered the silicon temperature of 18 K, where silicon has a zero thermal expansion coefficient resulting in negligible thermo-elastic

thermal noise in GW observatories [30]. The accommodation coefficient for helium on silicon cryogenic test masses has values greater than 0.7 below 20 K. Notably, for 18 K we found $\alpha = 0.74 \pm 0.03$.

Our conceptual setup of using a heat exchange gas to cool suspended test mass mirror in future GW observatories [21], assumed an accommodation coefficient of 0.6. This work shows that for silicon temperatures of 18 K gas cooling is approximately 23% more efficient than previously discussed. In the context of optimizing ground-based interferometric detectors like the Einstein Telescope, this study highlights the potential benefits of incorporating gas cooling as an additional tool in the design process. By reducing building costs or increasing sensitivity and robustness, such a system could contribute to advancing our ability to detect GWs.

The potential of gas cooling in third-generation GW detectors is increased, and the consideration of implementing this technique should be continued. For a given gas cooling power, the added mirror displacement noise decreases with the square of the mirror mass and a quartic dependency on frequency. This makes gas cooling a potential cooling solution, especially for mirror masses greater than 200 kg or detectors targeting signal frequencies above a few hundred hertz. Due to technical limitations, our setup only allowed the determination of α between 11 K and 30 K. However, knowledge of the accommodation coefficient in a greater range of temperatures may become necessary, as detector configurations using test mass temperatures of 77 K and 123 K have been proposed [11].

Data availability statement

The data cannot be made publicly available upon publication because the cost of preparing, depositing and hosting the data would be prohibitive within the terms of this research project. The data that support the findings of this study are available upon reasonable request from the authors.

Acknowledgments

This work was supported and partly financed (A F, N S) by the DFG under Germany's Excellence Strategy EXC 2121 'Quantum Universe'—390833306. Figures created with matplotlib [31] and the python package uncertainties [32].

ORCID iDs

Alexander Franke https://orcid.org/0000-0002-4843-1112
Christoph Reinhardt https://orcid.org/0000-0002-5976-4430
Roman Schnabel https://orcid.org/0000-0003-2896-4218

References

[1] Abbott B P *et al* (LIGO Scientific Collaboration and Virgo Collaboration) 2016 Observation of gravitational waves from a binary black hole merger *Phys. Rev. Lett.* **116** 061102
[2] Aasi J *et al* 2015 Advanced LIGO *Class. Quantum Grav.* **32** 074001
[3] Acernese F *et al* 2014 Advanced Virgo: a second-generation interferometric gravitational wave detector *Class. Quantum Grav.* **32** 024001
[4] Akutsu T *et al* 2019 KAGRA collaboration KAGRA: 2.5 generation interferometric gravitational wave detector *Nat. Astron.* **3** 35–40

[5] Gais J, Ng K K Y, Seo E, Wong K W K and Li T G F 2022 Inferring the intermediate-mass black hole number density from gravitational-wave lensing statistics *Astrophys. J. Lett.* **932** L4
[6] Agazie G *et al* (The NANOGrav Collaboration) 2023 The nanograv 15 yr data set: evidence for a gravitational-wave background *Astrophys. J. Lett.* **951** L8
[7] The LIGO Scientific Collaboration and The Virgo Collaboration, The 1M2H Collaboration, The Dark Energy Camera GW-EM Collaboration and the DES Collaboration, The DLT40 Collaboration, The Las Cumbres Observatory Collaboration, The VINROUGE Collaboration and The MASTER Collaboration 2017 A gravitational-wave standard siren measurement of the Hubble constant *Nature* **551** 85–88
[8] Abernathy M *et al* 2011 *Einstein Gravitational Wave Telescope Conceptual Design Study*
[9] ET Steering Committee Editorial Team 2020 *Einstein Telescope Design Report Update 2020*
[10] Reitze D *et al* 2019 Cosmic explorer: the U.S. contribution to gravitational-wave astronomy beyond LIGO *Bull. AAS* **51** 7
[11] Ackley K *et al* 2020 Neutron star extreme matter observatory: a kilohertz-band gravitational-wave detector in the global network *Publ. Astron. Soc. Aust.* **37** e047
[12] Adhikari R *et al* 2020 A cryogenic silicon interferometer for gravitational-wave detection *Class. Quantum Grav.* **37** 165003
[13] Miller J, Barsotti L, Vitale S, Fritschel P, Evans M and Sigg D 2015 Prospects for doubling the range of advanced ligo *Phys. Rev.* D **91** 062005
[14] Adhikari R X, Brooks A, Shapiro B, McClelland D, Gustafson E K, Mitrofanov V, Arai K, Wipf C and Bonilla E 2023 LIGO voyager upgrade: design concept (available at: https://docs.ligo.org/voyager/voyagerwhitepaper/main.pdf)
[15] Buikema A *et al* 2020 Sensitivity and performance of the Advanced LIGO detectors in the third observing run *Phys. Rev.* D **102** 062003
[16] Acernese F *et al* 2020 Advanced virgo status *J. Phys.: Conf. Ser.* **1342** 012010
[17] Somiya K 2012 Detector configuration of KAGRA – the Japanese cryogenic gra-vitational-wave detector *Class. Quantum Grav.* **29** 124007
[18] Akutsu T *et al* 2020 Overview of KAGRA: detector design and construction history *Prog. Theor. Exp. Phys.* **2021** 05A101
[19] The ETpathfinder Team 2020 (available at: https://www.etpathfinder.eu/wp-content/uploads/2020/03/ETpathfinder-Design-Report.pdf)
[20] Utina A *et al* 2022 ETpathfinder: a cryogenic testbed for interferometric gravitational-wave detectors *Class. Quantum Grav.* **39** 215008
[21] Reinhardt C, Franke A L A, Schaffran J, Schnabel R M and Lindner A 2021 Gas cooling of test masses for future gravitational-wave observatories *Class. Quantum Grav.* **38** 185003
[22] Trott W M, Casta neda J N, Torczynski J R, Gallis M A and Rader D J 2011 An experimental assembly for precise measurement of thermal accommodation coefficients *Rev. Sci. Instrum.* **82** 035120
[23] Corruccini R 1959 Gaseous heat conduction at low pressures and temperatures *Vacuum* **7-8** 19–29
[24] Gombosi T I and Gombosi A 1994 *Gaskinetic Theory* vol 9 (Cambridge University Press)
[25] Czochralski J 1918 Ein neues Verfahren zur Messung der Kristallisationsgeschwindigkeit der Metalle *Z. Phys. Chem.* **92** 219–21
[26] Simon N J, Drexler E S and Reed R P 1992 Properties of copper and copper alloys at cryogenic temperatures *Final Report* (National Institute of Standards and Technology)
[27] Swenson C A 1983 Recommended values for the thermal expansivity of silicon from 0 to 1000 K *J. Phys. Chem. Ref. Data* **12** 179–82
[28] Choi Y and Kim D L 2012 Thermal property of insulating material at cryogenic temperature *J. Mech. Sci. Technol.* **26** 2125–8
[29] Ekin J 2006 *Experimental Techniques for Low-Temperature Measurements: Cryostat Design, Material Properties and Superconductor Critical-Current Testing* 1st edn (Oxford University Press)
[30] Rowan S, Byer R L, Fejer M M, Route R K, Cagnoli G, Crooks D R, Hough J, Sneddon P H and Winkler W 2003 Test mass materials for a new generation of gravitational wave detectors *Proc. SPIE* **4856** 292–7
[31] Hunter J D M 2007 A 2D graphics environment *Comput. Sci. Eng.* **9** 90–95
[32] Lebigot E O 2024 Uncertainties: a python package for calculations with uncertainties (available at: http://pythonhosted.org/uncertainties/)